Article

Evaluating Fractal Damage and Acoustic Emissions of Soft Rock–Coal Combinations in a Deep Mining Area

Bin Liang [1], Dong Wang [1,2,*], Yujing Jiang [1], Xiaoming Sun [2], Hengjie Luan [1,3], Changsheng Wang [1], Ling Dong [1] and Lugen Chen [1]

1   State Key Laboratory of Mining Disaster Prevention and Control Co-Founded by Shandong Province and the Ministry of Science and Technology, Shandong University of Science and Technology, Qingdao 266590, China; lblb9924@163.com (B.L.)
2   State Key Laboratory for Geomechanics and Deep Underground Engineering, China University of Mining and Technology, Beijing 100083, China
3   Inner Mongolia Shanghaimiao Mining Co., Ltd., Ordos 016299, China
*   Correspondence: wdwinter@163.com; Tel.: +86-156-2102-9309

Abstract: Weakly cemented soft rock mines in the Ordos Basin are susceptible to mining disasters, including roof collapse and substantial deformation of surrounding rocks, during coal mining operations. Researching the damage characteristics of structures composed of low-strength "soft rock–coal" combinations is crucial for effectively preventing and controlling disasters in deep soft rock mining. To investigate the fractal damage characteristics of soft rock–coal combinations with different height ratios, uniaxial compression tests were conducted on specimens containing soft rock percentages of 20%, 40%, 50%, 60%, and 80%. The results show that the uniaxial compressive strength and modulus of elasticity of the soft rock–coal combinations increased with increasing proportions of soft rock. The soft rock–coal combination was clearly segmented, and the 40%, 50%, and 60% soft rock–coal combinations had good self-similarity. The fractal dimensions were 2.374, 2.508 and 2.586, which are all within the interval [2, 3]. When the percentage of soft rock was 20%, the specimen damage yielded flaky coal bodies with smaller grain size, whereas the coal–rock interface was spalled by small conical rock bodies. As the soft rock proportion increased, the percentage mass of fragments with particle size greater than 20 mm increased from 83.34% to 94.15%. The failure mode in soft rock–coal combinations is primarily attributed to the partial tensile splitting of the coal body. As the proportion of soft rock increased, there was a gradual reduction in the extent of coal body damage. Moreover, the acoustic emission absolute energies and counts decreased as the proportion of soft rock increased. The acoustic emission energy was reduced from 2.46×10^9 attoJ to 3.41×10^8 attoJ, and the acoustic emission counts were reduced from 18,276 to 7852.

Keywords: deep mining area; soft rock–coal combinations; fractal damage; acoustic emission

1. Introduction

Currently, coal remains the primary energy source for meeting China's energy requirements, a position unlikely to change in the foreseeable future [1]. With the deepening of mining operations, deep soft rock mines encounter persistent high stress and multiple hazardous environments, posing significant threats to the safe extraction of coal resources [2–4]. The Ordos Basin, located in the western region of northern China, boasts substantial coal reserves. However, the complexity of mining conditions challenges operations. This complexity is due to the large resource burial depth. The surrounding rock of weakly cemented soft rock mines is composed of weakly soft rock, which has high water content and contains much loose material such as sandy mudstone, siltstone, and muddy sandstone [5]. Coal mine disasters, including roof collapse, significant deformation of surrounding rocks and water surges, frequently occur in soft rock mines [6,7]. These disasters are closely associated with the mechanical behavior of the entire coal–rock system [8–10]. Specifically, the unique

structural characteristics of soft rock–coal combinations, composed of weakly cemented soft rock layers and coal seams in the top and bottom strata, complicate the deformation and destabilization mechanisms of coal rock bodies in deep soft rock mines.

Scholars worldwide have conducted extensive studies on the mechanical properties of coal–rock combinations and their fractal characteristics. Petukhov and Linkov [11] first analyzed the stability of two-body systems and "roof bottom slab coal body" systems. Zhou et al. [12] and Chen et al. [13] explored the energy distribution of coal–rock assemblage specimens with different height ratios and diameters prior to load damage. Yang et al. [14] used Xin'an coal mine as an example to study the large deformation damage mechanism of deep soft rock roadway. Ma et al. [15] investigated the mechanical properties of rock–coal–rock composites with different thicknesses of inclined coal seams in conjunction with numerical simulations. Song et al. [16] investigated the strength characteristics and progressive damage mechanism of soft rock–coal assemblage, reporting on interface effects. Daraei et al. [17] predicted the limestone static elastic modulus from seismic tests. Yin et al. [18] investigated the uniaxial compressive damage of a composite specimen of coal from persistent nodal caprock–coal–surface rock by numerical simulation. Najm et al. [19] predicted extrusion and rockburst damage through empirical and numerical analysis. Zuo et al. [20] investigated the mechanical properties and rockburst propensity of different coal–rock combinations. Gong et al. [21] elucidated the effect of the loading rate on the impact propensity of combined specimens. Xie et al. [22] used rock mechanics tests and theoretical studies to analyze the fractal characteristics of rock fragments and derived a fractal model of crack bifurcation. Chen et al. [23] investigated the fractal characteristics of coal–rock combinations under different loading rates. Feng et al. [24] studied the acoustic emission characteristics and fragmentation distribution of coal samples with varying water contents. Li, Y et al. [25] examined the fractal characteristics of coal sample fragments under uniaxial cyclic loading and unloading. Li, J et al. [26] analyzed the evolutionary pattern of sandstone damage and its fractal characteristics. Zhou et al. [27] and Kong et al. [28] conducted a study of the acoustic emission characteristics.

Most research results focus on the coal–rock combination mode, mechanical properties, deformation, damage law, and energy evolution. They are predominantly based on the hard rock and soft coal combination model, where the strength of rock significantly surpasses that of coal. The roof and floor areas of the coal seams in the Ordos Shanghai Miao Mine consist mainly of low-strength soft rocks. Studies on this particular coal–rock system are limited. Therefore, this study involved conducting uniaxial compression experiments on "soft rock–coal" combinations with varying ratios of soft rock. The damage fragments of the combination specimens were quantified, and their fractal characteristics were analyzed. At the same time acoustic emission was used to study the damage characteristics. This investigation aims to provide a theoretical basis for understanding and preventing mining disasters in deep soft rock mines.

2. Geological Background

The Ordos Shanghaimiao, situated at the southwest end of the Ordos Plateau and to the west of the Mao Wusu Desert, lies at an altitude of 1300–1400 m. The administrative area falls under the jurisdiction of the Shanghaimiao Town of Otog Banner. The location of the Ordos Shanghaimiao mine is shown in Figure 1. As per the Summary Report of the Western Coal Geological Exploration of the Shanghaimiao Mining Area, Otog Banner, Inner Mongolia Autonomous Region, the cumulative resources of the mining area are confirmed to be 1574.29 Mt, with predicted resources amounting to 263.49 Mt. The coal seams in the Shanghaimiao mine area, noted for their depth and abundant groundwater, primarily belong to the Jurassic Middle Tong Yan'an Formation (J2y). The shaft field of Shanghaimiao No.1 Mine has a length of about 12.5 km from north to south, with 10 seams of recoverable and partially recoverable coal, and the total thickness of recoverable coal seams is 21.60 m. Hole C1 is located in the central part of the Shanghaimiao No.1 well field, with a depth of 464.45 m, and the stratigraphic histogram is shown in Figure 2. Predominantly, the

coal system rocks are sandy mudstone, siltstone, and muddy sandstone weakly cemented soft rocks. The soft rocks are primarily composed of minerals such as quartz, potassium feldspar, plagioclase, and clay minerals. Figure 3 exhibits the cathodoluminescence image of a muddy sandstone specimen.
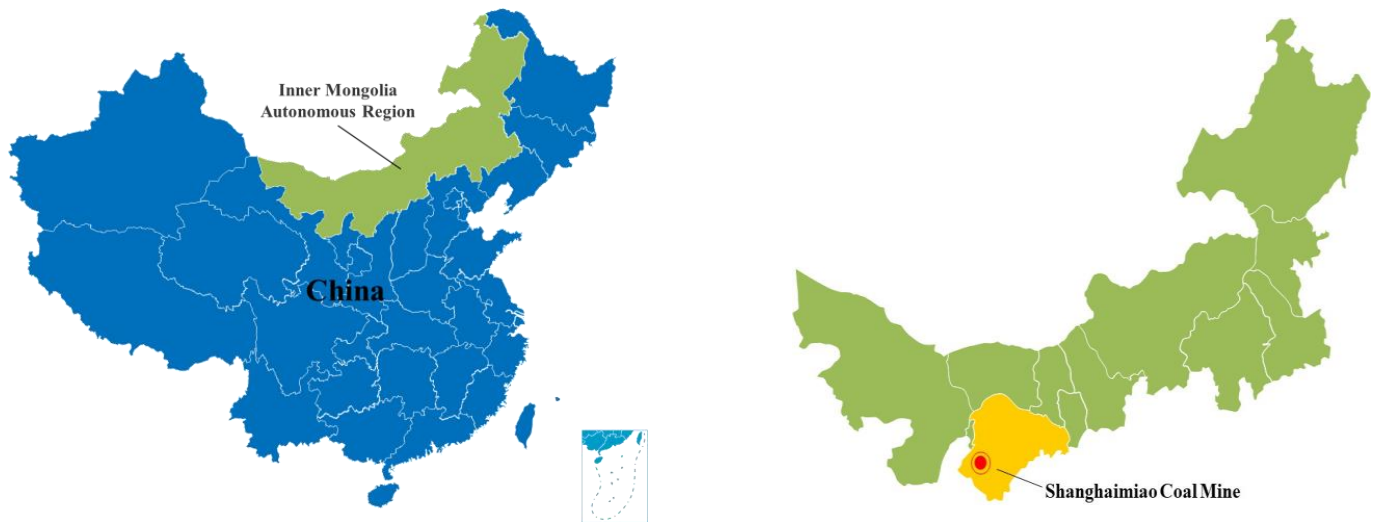

Figure 1. Ordos Shanghaimiao mine location map. The green represents the Inner Mongolia Autonomous Region and the red represents the Shanghaimiao Coal Mine.
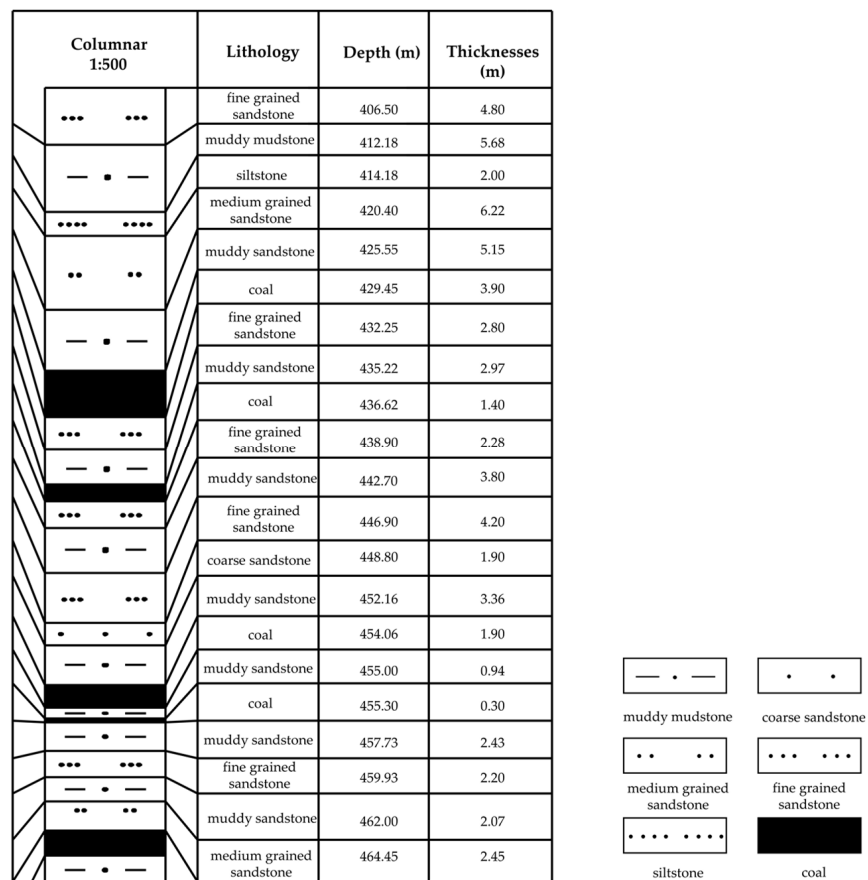

Columnar 1:500	Lithology	Depth (m)	Thicknesses (m)
	fine grained sandstone	406.50	4.80
	muddy mudstone	412.18	5.68
	siltstone	414.18	2.00
	medium grained sandstone	420.40	6.22
	muddy sandstone	425.55	5.15
	coal	429.45	3.90
	fine grained sandstone	432.25	2.80
	muddy sandstone	435.22	2.97
	coal	436.62	1.40
	fine grained sandstone	438.90	2.28
	muddy sandstone	442.70	3.80
	fine grained sandstone	446.90	4.20
	coarse sandstone	448.80	1.90
	muddy sandstone	452.16	3.36
	coal	454.06	1.90
	muddy sandstone	455.00	0.94
	coal	455.30	0.30
	muddy sandstone	457.73	2.43
	fine grained sandstone	459.93	2.20
	muddy sandstone	462.00	2.07
	medium grained sandstone	464.45	2.45

Legend: muddy mudstone, coarse sandstone, medium grained sandstone, fine grained sandstone, siltstone, coal

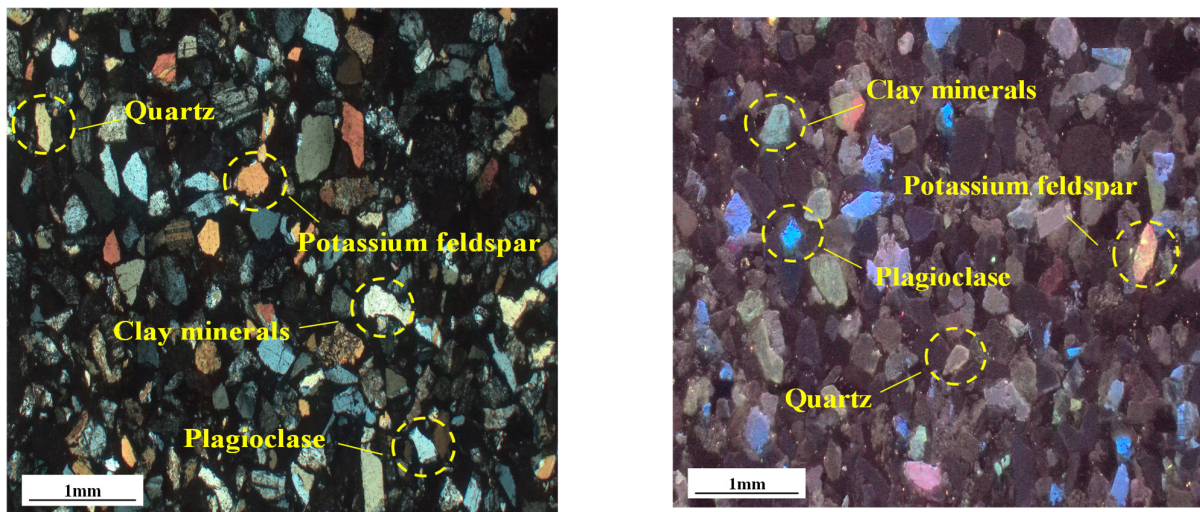**Figure 2.** Stratigraphic histogram of Hole C1.

Figure 3. Cathodoluminescence image.

3. Experimental Test Methods and Results

3.1. Sample Preparation

The samples for this study were obtained from a coal seam and its roof rock of muddy sandstone in the Shanghaimiao coal mine, Ordos. The rock and coal samples were converted into cylindrical standard specimens of size φ 50 mm $\times$ 100 mm (the non-parallelism value between the two end surfaces should not exceed 0.02 mm) based on different soft rock percentages (20%, 40%, 50%, 60%, and 80%, respectively) [29]. A standard specimen is depicted in Figure 4. Different coal–rock combinations may have different compositions, which include coal content, and mineral content. These compositional differences may lead to differences in contact strength and stiffness. Given the need for high strength and thin thickness at the interface of coal–rock combinations, high-strength water-soluble white latex is employed as a binder. This latex offers benefits including rapid curing, superior bond strength, and enhanced durability of the bonding layer. A small quantity of white latex is evenly applied at the coal–rock interface, and subsequently left to set for 24 h.

Figure 4. Soft rock–coal combinations of different height ratios.

3.2. Test Equipment and Methods

The uniaxial compression test for this experiment was conducted using a self-developed creep-disturbance dynamic shock loading test system (as shown in Figure 5). The system consists of a host loading system, a hydraulic pump station system, an axial hydraulic control system, and a data acquisition system. The static load range of the main loading

system is from 0 to 800 kN. The power loading unit can exert a maximum axial load of 100 kN, with a maximum axial loading stroke of 150 mm. The displacement control rate ranges from 0.1 to 150 mm/min, and the measurement control accuracy achieves $\pm 0.5\%$ of the indicated value. Axial stress and axial displacement were accurately monitored and recorded utilizing pressure sensors and magnetic displacement sensors. The experiments were conducted through displacement loading, with the axial loading rate set at 0.1 mm/min until the specimen underwent complete failure.
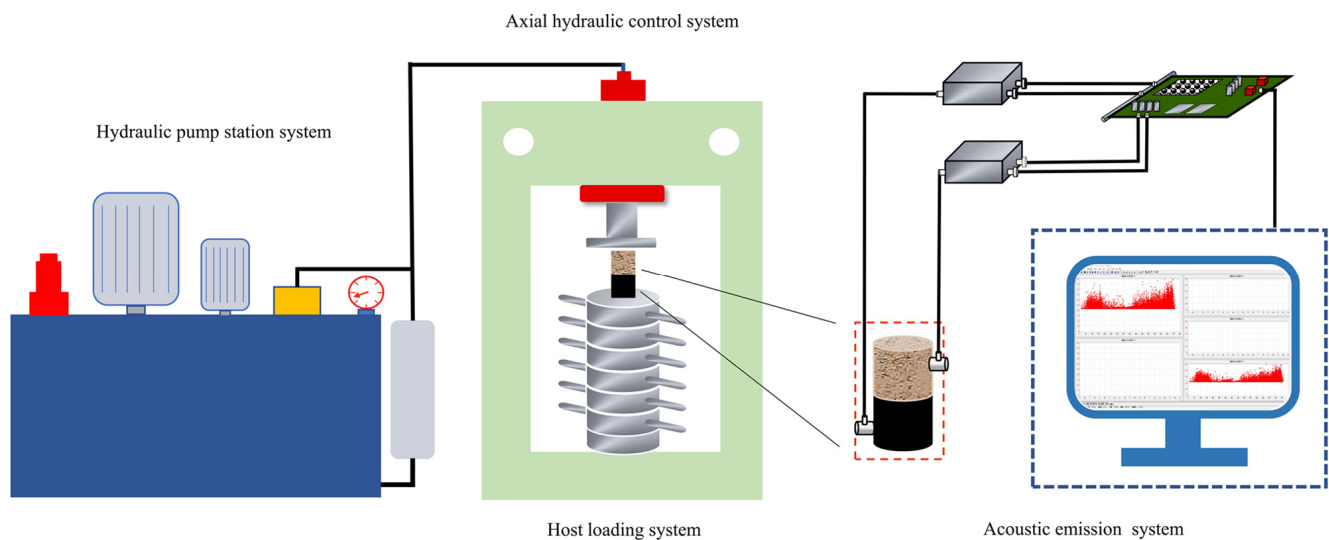

Figure 5. Schematic diagram of creep-disturbance dynamic loading system. The green represents the host loading system and the blue represents the hydraulic pump station system.

The acoustic emission signals were monitored employing a Sensor Highway II acoustic emission unit (AE) from Physical Acoustic Corporation, West Windsor Township, NJ, USA. This system enables real-time acoustic emission feature parameter extraction, waveform acquisition, and processing. The AE system threshold was set to 43 dB, and the sampling frequency was fixed at 1 MHz. Channels 1 and 5 were established, each corresponding to one independent acoustic emission probe and preamplifier, amplifying the signal 40 times. To mitigate the friction impact between the transducer probe and the specimen end face on the test results, a coupling agent was uniformly applied at the specimen port and probe contact position, and tape was used for secure fixing. An acoustic emission break lead coupling test was performed before initiating the test to confirm the amplitude signal of each probe was above 90 dB.

3.3. Experimental Results

Prior to the uniaxial compression test of the soft rock–coal combinations, a separate uniaxial compression test was conducted on muddy sandstone and coal samples (the columns had a diameter × height of 50 mm × 100 mm) from the Shanghaimiao Mine. The uniaxial compressive strengths were found to be 24.8 MPa and 16.8 MPa, respectively. Soft rock–coal combinations with varying rock-to-coal ratios (20%, 40%, 50%, 60%, and 80%) were then subjected to uniaxial compression tests. The results are presented in Table 1. Figure 6 illustrates the stress–strain curve (a), peak strain (b), uniaxial compressive strength (c), and elastic modulus curves (d) for different soft rock–coal combinations.

Table 1. Uniaxial compression experimental results of different soft rock–coal combinations.

Proportions of Soft Rocks	Uniaxial Compressive Strength (MPa)	Modulus of Elasticity (GPa)	Peak Strain (%)	Destruction Mode
20%	17.24	2.07	1.0363	tensile splitting
40%	19.65	2.50	0.9941	tensile splitting
50%	20.10	2.64	0.9030	tensile splitting
60%	20.68	2.67	0.8764	tensile splitting
80%	21.72	3.23	0.7856	tensile splitting
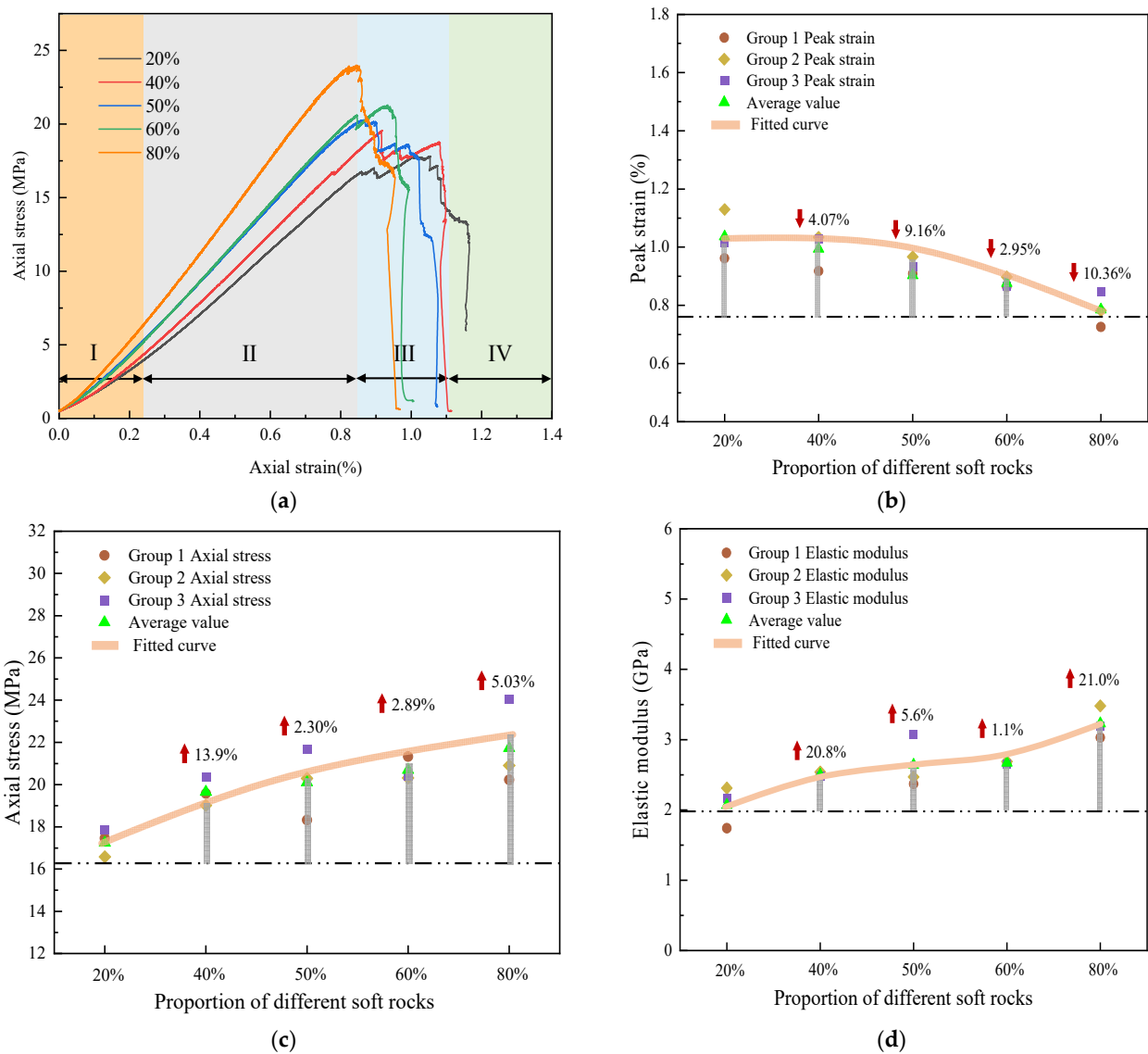
Figure 6. Stress–strain (**a**), peak strain (**b**), uniaxial compressive strength (**c**), and modulus of elasticity curves (**d**) for different soft rock–coal combinations. Figure (**b**–**d**) dashed lines as baselines.

Analyzing the stress–strain curves of the soft rock–coal assemblies, it is evident that the specimens, regardless of the soft rock occupancy ratio, display an initial compression-density stage (I), a quasi-linear elasticity stage (II), a plastic yielding stage (III), and a post-peak damage stage (IV) during the loading process. The overall shape of the curves resembles the stress–strain curve of an individual coal sample, with both exhibiting a stepwise downward trend in the post-peak damage stage. As the percentage of soft rock

in the assemblage increases, plastic damage escalates, and brittle damage decreases in the damage phase following the curve's peak. Chen et al. [30] suggested that in the post-peak stage of the stress–strain curve of a coal–rock assembly, a greater rock-to-coal height ratio led to increased plastic damage in the assembly specimen and increased peak stress. This is attributed to coal–rock interface effects [20]. The derived stresses in the muddy sandstone at the coal–rock interface are tensile stresses, which facilitate the damage to the assembly. Conversely, the derived stresses in the coal section are compressive stresses, mitigating the damage of the assembly. Hence, as the proportion of soft rock increases, the coal body portion is more constrained by compressive stress, and the intensity of the coal body damage process is weaker.

As indicated in Table 1 and Figure 6, the mean values for uniaxial compressive strengths for varying proportions of soft rock and coal (20%, 40%, 50%, 60%, and 80% soft rock) within the Shanghaimiao mining area are 17.24 MPa, 19.65 MPa, 20.10 MPa, 20.68 MPa, and 21.72 MPa, respectively. The average elasticity moduli are 2.07 GPa, 2.50 GPa, 2.64 GPa, 2.67 GPa, and 3.23 GPa, and the average peak strains are 1.0363, 0.9941, 0.9030, 0.8764, and 0.7856, respectively.

The uniaxial compressive strength of these soft rock–coal combinations falls within the range of strength between rock and coal. Both uniaxial compressive strength and the modulus of elasticity in these combinations display positive correlations with the increasing percentage of soft rock. The uniaxial compressive strength elevates by 13.9%, 2.30%, 2.89%, and 5.03%, whereas the modulus of elasticity climbs by 20.8%, 5.6%, 1.1%, and 21.0%, respectively. Conversely, the peak strain of the soft rock–coal composite exhibits a decreasing trend with the growing percentage of soft rock, reducing by 4.07%, 9.16%, 2.95%, and 10.36%, respectively. The variations in the strength properties of the various soft rock–coal combinations arise from the interaction between the soft rock and coal components.

4. Fractal Damage Characteristics

4.1. Methods of Classification of Fragments

Following the crushing of soft rock–coal combinations, fragments of varying sizes and qualities are produced. To conduct a precise and reasoned analysis of the distribution characteristics of these fragments, it is essential to employ appropriate statistical research methodologies. This study categorizes assemblage fragments into four groups based on their size: particles (<5 mm), small particles (<10 mm), medium particles (<20 mm), and large particles (>20 mm). The classification of these tiny particles into three subcategories was implemented to enhance the examination of fragment distribution, considering the substantial quantity resulting from the destruction of coal samples. Table 2 provides the classification standards and analysis methods for the assemblage fragments.

Table 2. Classification criteria and analysis methods of the combined body fragments.

Number	Fragmentation Category	Particle Size Range (mm)	Research Methodology
1	Particulate	<1.25 (1.25, 2.5) (2.5, 5)	Weighing mass
2	Small grains	(5, 10)	Weighing mass
3	Medium grain	(10, 20)	Weighing mass
4	Large grains	>20	Weighing mass

Upon uniaxial compression testing, soft rock–coal combinations were sieved, weighed, and sorted. Sample fragments post-axial loading were sieved using circular hole sieves. The sieving equipment consisted of five different aperture multi-stage sieves, with diameters of 20 mm, 10 mm, 5 mm, 2.5 mm, and 1.25 mm. Particles from each sieve class were weighed

using a high-precision electronic scale and counted to obtain the fragment number in each interval. The remaining fragments were collectively measured using vernier calipers to establish sizes.

4.2. Characterization of Damage Fragment Distribution

When a coal–rock combination specimen is crushed, there is a certain connection between the fractals and fragments. The broken fragments can be regarded as fragments with fractal characteristics. By studying the fractal characteristics of the broken fragments, we can gain a deeper understanding of the crushing mechanism of the coal–rock combination specimen and its mechanical properties, which can provide certain theoretical support for the mining, blasting, and geologic hazards of the coal–rock engineering. In order to study the change rule of the mechanical properties of the soft rock–coal combinations subjected to load damage and to investigate the distribution characteristics of its broken blocks, different soft rock–coal combinations of specimens corresponding to the six kinds of broken block size, broken block sieving, and organization were analyzed, as shown in Figure 7.
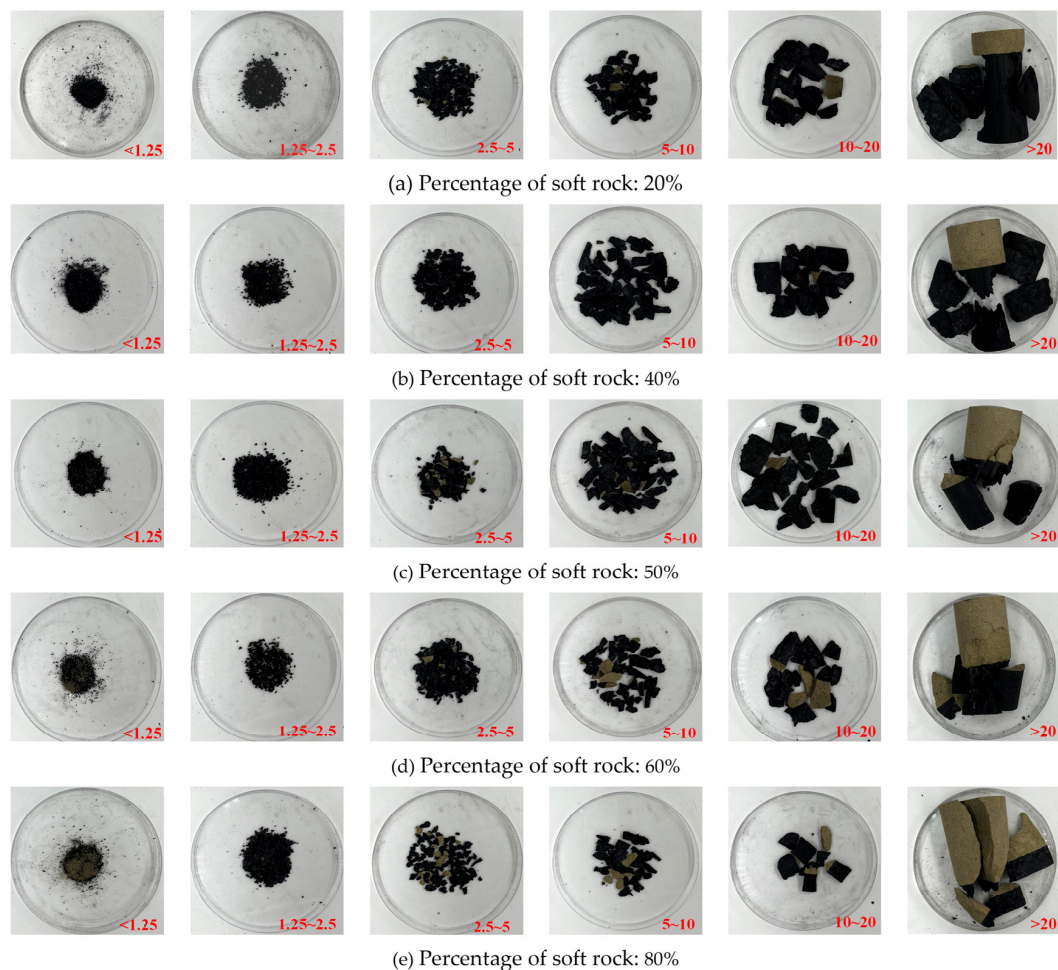

(a) Percentage of soft rock: 20%

(b) Percentage of soft rock: 40%

(c) Percentage of soft rock: 50%

(d) Percentage of soft rock: 60%

(e) Percentage of soft rock: 80%

Figure 7. Fractal results for different coal–rock combinations.

Figure 7 demonstrates that the damage within different soft rock–coal combinations is primarily governed by coal body splitting. In complete combinations, the coal body sustains more damage than the rock body, with rock body damage primarily occurring as small pieces of rock spalling at the coal–rock interface, along with a minor amount of powdery particles. The assemblage with a 20% soft rock composition displays substantial coal body fragmentation, with a high number of particles and medium grains. Rock destruction is minimal, with only a few small rock pieces breaking off at the coal–rock interface.

The coal–rock combinations at 40%, 50%, and 60% soft rock composition are all dominated by coal body destruction, with a high number of medium grains and a small amount of powdered rock particles present in the assemblage particles. The number of rock fragments incrementally increases, and the fragments around the coal–rock interface are prevalent. The combination with 80% soft rock shows cleavage cracks throughout, and the coal body fragments appear in a flaky structure. Post-destruction at the coal–rock interface, the fragments remain in the form of coal–rock combinations, and the coal body in the assemblage roughly exhibits a conical shape. As the soft rock percentage increases, the destruction in the rock portion of the different soft rock combinations progressively increases, leading to a rise in rock fragments and a decline in coal fragments.

4.3. Characterization of Fragment Quality

Table 3 illustrates the mass percentage distribution intervals of fragmentation block sizes in different soft rock–coal combinations, with the results plotted in Figure 8. Table 3 and Figure 8 indicate that as the proportion of soft rock increases, the mass percentage of fragments larger than 20 mm gradually increases from 83.34% at 20% soft rock, incrementing by 1.61%, 2.74%, 4.66%, and 10.71%. As the proportion of soft rock rises, the mass percentage of fragments smaller than 20 mm shows a general decrease. At a lower percentage of soft rock, coal body destruction is greater, generating a significant number of particles. As the soft rock percentage elevates, destruction in the rock body part increasingly produces larger blocks, which constitute a larger percentage of the mass.

Table 3. Distribution intervals of block size and mass percentage of assemblage fragments.

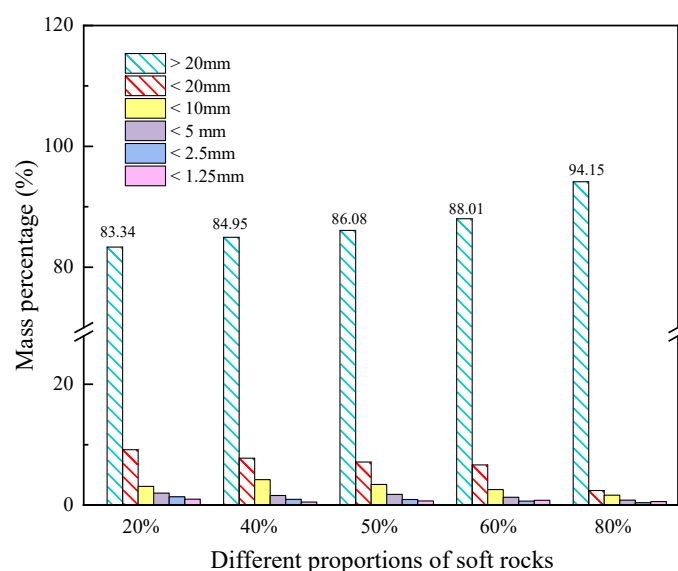| Size (mm)	Rock Percentage (%)				
	20%	**40%**	**50%**	**60%**	**80%**
<1.25	0.99	0.51	0.69	0.81	0.58
(1.25, 2.5)	1.38	0.95	0.91	0.67	0.40
(2.5, 5)	2.00	1.60	1.78	1.30	0.84
(5, 10)	3.10	4.23	3.42	2.57	1.63
(10, 20)	9.19	7.76	7.12	6.64	2.40
>20	83.34	84.95	86.08	88.01	94.15

Figure 8. Percentage of fragmentation block size for different soft rock–coal combinations.

4.4. Calculation of Fragmentation

Shape theory serves as a research instrument for the quantitative characterization of morphological information pertaining to the fracture surfaces of coal rocks and the description of shattered fragments. The fractal dimension (*D*) is a useful metric for discussing the irregularities of complex self-similar shapes [22]. Owing to the irregularity and sheer number of fragments resulting from axially loaded coal–rock combinations, especially those of smaller particle sizes, counting the number accurately becomes challenging. To address this difficulty, the distribution pattern of fragments post-crushing can be analyzed using the G-G-S model [31,32]. The relationship between mass and size of shattered pieces is computed using the G-G-S model, enabling the determination of the fractal dimension (*D*) post-crushing. Doing so improves the characterization of coal–rock assembly crushing.

The fractal dimension (*D*) is calculated as follows:

$$D = \frac{ln N_r}{ln(1/r)} \tag{1}$$

$$N_r \propto r^{-D}$$

where *r* is the particle size of a given fragment and N_r is the number of fragments.

The G-G-S model is calculated [33] as follows:

$$y = \left(\frac{r}{R}\right)^b \tag{2}$$

where *r* is the particle size of a particular clump, *R* is the maximum value of the particle size of the fragment, and *b* is the regression coefficient.

From the above equation, we can derive:

$$ln\frac{M_r}{M} = (3 - D)ln\frac{r}{R} \tag{3}$$

where M_r is the cumulative mass of fragments with a particle size smaller than *r* and *M* is the mass of fragments.

The fractal dimension (*D*) can be determined by logarithmically processing and linearly fitting the test data with a slope of (3 − *D*), as per Equation (3).

Table 4 shows the $ln\frac{M_r}{M} - ln\frac{r}{R}$ relationships for the data processed from the crushed specimen post-uniaxial compressive loading.
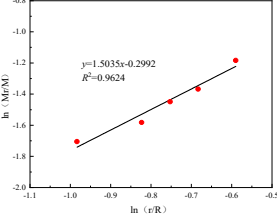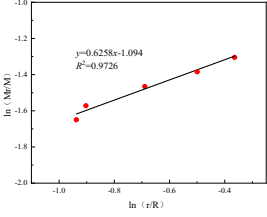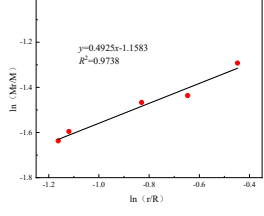
The table also shows that prior to test loading, the surfaces of different soft rock–coal combination specimens reveal no prominent primary cracks. The yellow dash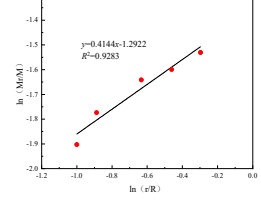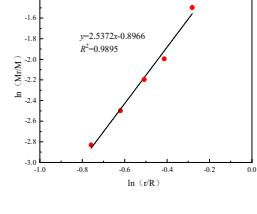ed line in the table indicates the main crack and the orange realization indicates the crack extension. The mode of destruction of the combination specimen is largely dominated by the splitting damage of the coal body when the proportion of soft rock is small. This results in a large conical block resulting from coal sample destruction and a significant proportion of smaller coal particles, with minor coal dust production. Concurrently, minor conical rock spalling occurs at the coal–rock interface.

As the proportion of soft rock increases, the primary damage mode shifts to the overall destabilization of the assembly, induced by coal body splitting and ejection. It typically manifests as several coherent splitting surfaces, accompanied by the ejection of flaky or thin coal lumps. The specimen's surface forms an evident "concave" damage surface, accompanied by a noticeable bursting sound from the coal sample during the experiment.

The damage degree of the rock body incrementally increases, influenced by the interface effect. The destruction of the coal body results in the appearance of penetrating cleavage cracks in the rock body, and the fragments are spalled off in the manner of the coal–rock assembly at the coal–rock interface. This results in a significant proportion of large flakes from the rock body. The combination specimen with 80% soft rock exhibits a

low degree of coal body destruction, with only small pieces of coal body breaking, and the rock body is partially dominated by pull and shear destruction.

Table 4. Combinatorial damage pattern and fractal dimension.

Percentage of Soft Rock	Destructive Pattern	Crack Pattern	Fitting the Curve	Calculation Results
20%			$y=1.5035x-0.2992$ $R^2=0.9624$	D = 1.496 R2 = 0.9624
40%			$y=0.6258x-1.094$ $R^2=0.9726$	D = 2.374 R2 = 0.9726
50%			$y=0.4925x-1.1583$ $R^2=0.9738$	D = 2.508 R2 = 0.9738
60%			$y=0.4144x-1.2922$ $R^2=0.9283$	D = 2.586 R2 = 0.9283
80%			$y=2.5372x-0.8966$ $R^2=0.9895$	D = 0.463 R2 = 0.9895

The results of the fractal dimension fitting reveal that the fractal dimension D = 0–3. With the increase in the proportion of soft rock, the fractal dimension of the assembly displays and increasing trend followed by a decreasing trend. The double logarithmic linear correlation of the 40%, 50%, and 60% combination specimens was robust, with squared R^2 linear fit coefficients ranging from 0.90 to 0.99. The fractal characteristics are significant, with fractal dimensions of 2.374, 2.508, and 2.586, which fall within the interval [2, 3], with a large proportion of small-sized fragments. The 20%, 40%, 50%, and 60% soft

rock percentage assembly specimen damage occurs predominantly in the coal body, with a minimal number of rock fragments.

Upon calculating the fractal dimension, it was observed that the assembly fractals are dominated by the coal body. This indicates that the energy absorbed by the assembly specimen as a whole is primarily used for the destruction of the coal body part [34], and the fractal dimension of the assembly crushing largely reflects the degree of destruction of the coal body part. The combination specimens with 80% soft rock have a small number of large-sized specimens, but they contribute significantly to their fractal dimension. Many researchers have posited that rock fragment self-similarity does not necessarily persist across the full range of block sizes. Feng et al. [24] argued that large-size fragments greatly influence the fractal dimension of coal samples with varying moisture contents. Li et al. [25] posited that rock fragments exhibit robust fractal properties for a range of sizes smaller than their size thresholds. Deng et al. [35] studied the fractalization of broken marble blocks under uniaxial loading, suggesting that the fractalization of broken blocks is segmented. Within these segmented intervals, the clastic fractal character is evident. The coal–rock combinations also manifest the same fractal segmentation nature of the fragments. The 80% soft rock specimens have a low fragment count and are dominated by large sizes of 50 mm or more. Calculations of the fractal dimensions are mainly in the form of coal–rock combinations with insignificant fractal features.

5. Acoustic Emission Characteristics of Soft Rock–Coal Combinations

The damage of the soft rock–coal combination is a result of the elastic strain energy accumulated within the specimen reaching its limit, which is then converted into mechanical energy released by the destruction of the combination [36,37]. Acoustic emission signals have proven to be more effective in characterizing the internal damage within the specimen. Based on the acoustic emission energy release characteristics, the peak value of the released energy at specimen damage, key point N^1, is extracted.

5.1. Characterization of Acoustic Emission Counting and Absolute Energy

The acoustic emission counts and absolute energy were selected as parameters to analyze the inherent connection between acoustic emission signals and specimen damage across different soft rock–coal combinations. The acoustic emission time–absolute energy-counts for various soft rock–coal combinations are displayed in Figure 9. The figure shows that the acoustic emission counts versus absolute energy curves have a distinct time-dependent characteristic, which is divided into three phases: the calm period (I), the active period (II), and the surge period (III). These correspond to the initial compression-density phase, the linear elasticity phase, and the post-peak damage phase, respectively, of the strength characterization. During the loading process, the internal fractures within the combined specimen are progressively compacted, a process indicated by fluctuations in the acoustic emission signal counts and absolute energy signals. The release energy of the combined specimen remains relatively low in the initial stages of loading, accounting for a minimal degree of damage. As the load increases, however, the acoustic emission signals from the combined specimen become more active during the online elastic phase, which signals minor damage within the specimen. The absolute energy and count of the acoustic emission reach their peak at the key point N^1, indicating that the extent of internal damage within the coal body is maximized during destabilization, accompanied by a significant release of energy, leading to observable, large-scale splitting damage in the coal body.

Table 5 demonstrates that the absolute energies at the key point N^1 for different chondrite–coal combinations are 2.46×10^9 attoJ, 1.36×10^9 attoJ, 1.03×10^9 attoJ, 3.93×10^8 attoJ, and 3.41×10^8 attoJ. With an increasing proportion of soft rock, the absolute energy and count of the acoustic emission exhibit a downward trend, suggesting that the acoustic emission signal of a soft rock–coal combination in a uniaxial compression experiment primarily serves to monitor the extent of damage within the coal body.
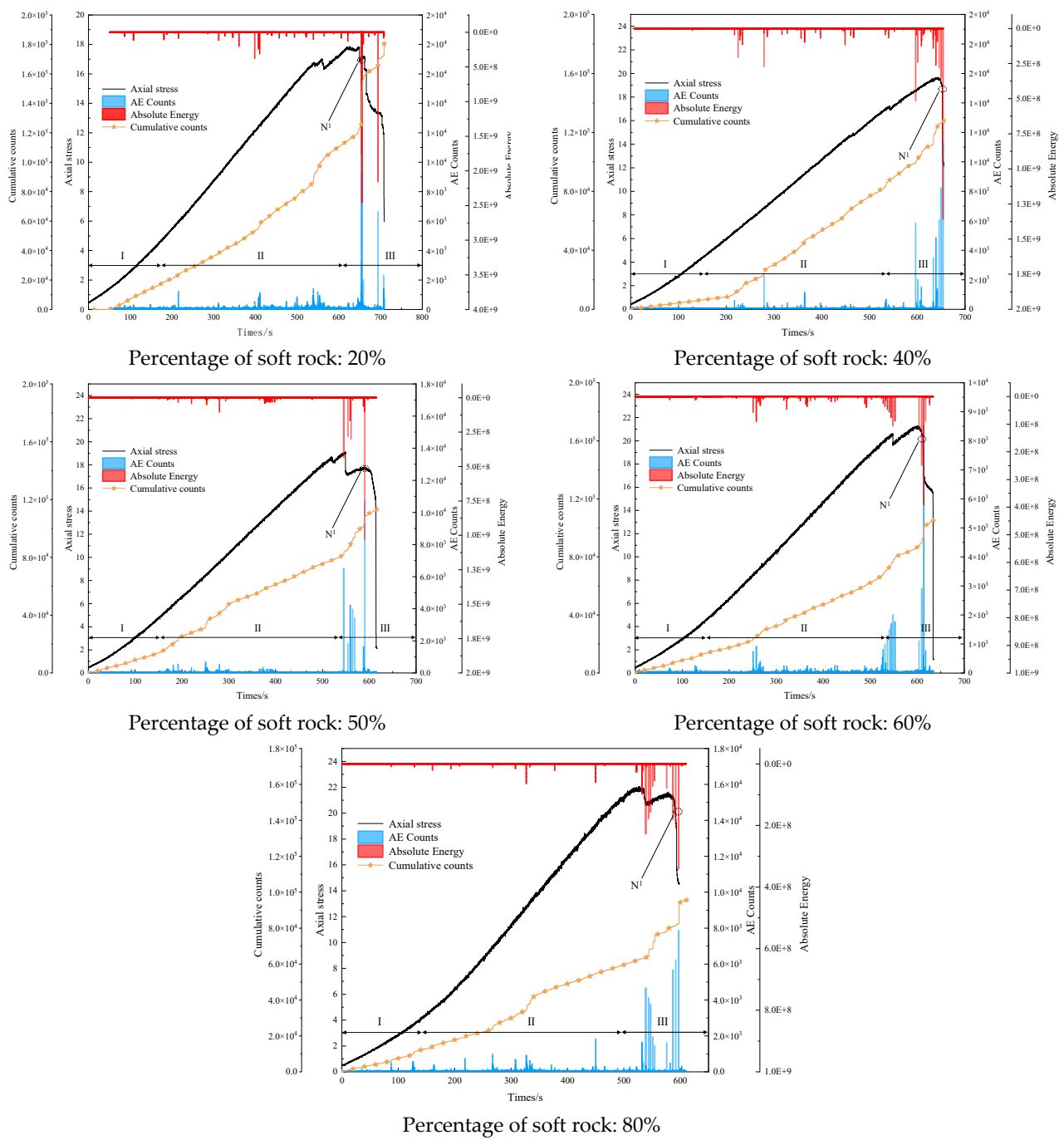
Percentage of soft rock: 20%

Percentage of soft rock: 40%

Percentage of soft rock: 50%

Percentage of soft rock: 60%

Percentage of soft rock: 80%

Figure 9. Acoustic emission time vs. absolute energy counts for different soft rock–coal combinations.

Table 5. Key point N^1 acoustic emission parameters and cumulative counts.

Percentage of Soft Rock	Absolute Energy (attoJ)	AE Counts	Cumulative Counts
20%	2.46×10^9	18,276	213,946
40%	1.36×10^9	11,283	128,026
50%	1.03×10^9	10,689	113,246
60%	3.93×10^8	8527	107,295
80%	3.41×10^8	7852	95,715

5.2. Acoustic Emission Waveform Characterization

During uniaxial loading, the specimen generates a continuous, random acoustic emission signal. This signal is transposed from the time domain to the frequency domain using Fast Fourier Transform, and MATLAB is utilized to create 3D maps of amplitude–frequency–time. As illustrated in Figure 10, the cusp corresponding to the amplitude in the map represents the main frequency characteristic value in soft rock–coal combinations where the proportion of soft rock ranges from 20% to 80%. The different colors in the figure represent the magnitude of the amplitude.
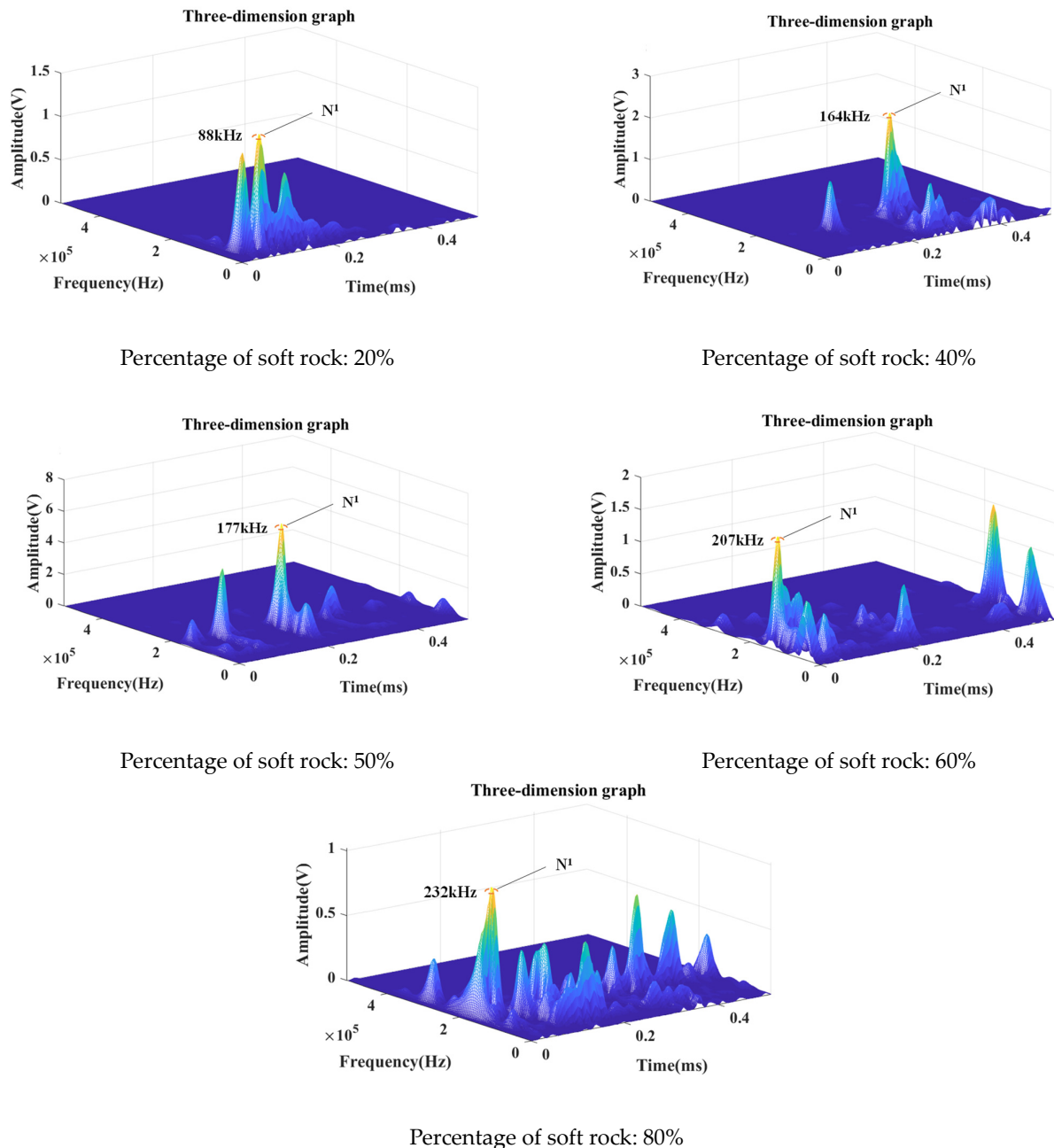

Percentage of soft rock: 20%

Percentage of soft rock: 40%

Percentage of soft rock: 50%

Percentage of soft rock: 60%

Percentage of soft rock: 80%

Figure 10. Main frequency characteristics of acoustic emissions for different samples at key points.

According to Figure 10 and Table 6, the main characteristic frequency values at the key point N^1 for different soft rock–coal combinations are 88 kHz, 164 kHz, 177 kHz, 207 kHz, and 232 kHz. The main characteristic frequency value ranges from 88 to 232 kHz and shows an upward trend with an increasing proportion of soft rock, indicating a gradual

decrease in the damage degree of the soft rock–coal combination. Reflecting the fractal characteristics of the combined specimen, the coal constitutes the primary component of the coal–rock system and is the first part to undergo destruction when destabilization of the surrounding rock of the soft rock roadway occurs. Thus, the supporting role of the coal body part should be augmented to prevent and mitigate disasters in deep soft rock mining.

Table 6. Main frequency value of key points of different samples.

Key Point	20%	40%	50%	60%	80%
N[1]	88 kHz	164 kHz	177 kHz	207 kHz	232 kHz

6. Conclusions

(1) The stages of deep soft rock–coal combinations under uniaxial loading include initial compaction, collinear elasticity, plastic yielding, and post-peak damage. With an increasing proportion of soft rock, the stepwise decreasing trend tends to slow down. The uniaxial compressive strength of the combination lies between that of monolithic rock and monolithic coal, correlates positively with the elasticity modulus, and increases with the proportion of soft rock. The uniaxial compressive strength elevates by 13.9%, 2.30%, 2.89%, and 5.03%, whereas the modulus of elasticity climbs by 20.8%, 5.6%, 1.1%, and 21.0%, respectively.

(2) In the deep mining area, the damage of soft rock–coal combinations with different height ratios are dominated by coal body splitting and tensile damage. The fractal characteristics of the combination specimens with 40%, 50% and 60% soft rock are significant with fractal dimensions of 2.374, 2.508 and 2.586, respectively, which are all within the interval [2, 3]. As the proportion of soft rock increases, the extent of damage inflicted on the coal body decreases, resulting in a concomitant reduction in the number of coal fragments. The fragmentation pattern exhibited by various combinations of soft rock and coal displays a sectional, fractal nature, with the dominant influence on the fractal characteristics derived from the coal body.

(3) The deep soft rock–coal combination specimens are characterized by a significant time-lapse in the acoustic emission counts and absolute energies, which can be divided into three phases: calm (I), active (II), and surge (III). The absolute acoustic emission energy and counts for the specimens peak at the key point N[1], implying that the internal damage of the coal body reaches a maximum during destabilization, and a substantial amount of energy is released, manifesting as large-scale splitting damage of the coal body. An increase in the proportion of soft rock leads to a reduction in both the absolute acoustic emission energy and counts.

(4) The range of the acoustic emission main characteristic frequency values for the deep soft rock–coal combination specimens spans from 88 to 232 kHz, with the values tending to increase as the proportion of soft rock increases. Coal–rock combinations with a soft rock percentage of 20% suffer large-scale destruction. In line with the strength characteristics and fractal features of the combination specimen, coal constitutes the primary component of the coal–rock system.

Author Contributions: Conceptualization, Y.J. and D.W.; methodology, B.L. and L.C.; validation, L.D., H.L. and C.W.; formal analysis, B.L.; writing—original draft preparation, B.L. and D.W.; writing—review and editing, D.W. and X.S. All authors have read and agreed to the published version of the manuscript.

Institutional Review Board Statement: Not applicable.

References

1. Chen, S.; Yin, D.; Zhang, B.; Ma, H.; Liu, X. Mechanical characteristics and progressive failure mechanism of roof-coal pillar structure. *Chin. J. Rock Mech. Eng.* **2017**, *36*, 1588–1598.
2. Xie, H.; Gao, F.; Ju, Y. Research and development of rock mechanics in deep ground engineering. *Chin. J. Rock Mech. Eng.* **2015**, *34*, 2161–2178.
3. Sun, X.; Wang, D.; Feng, J.; Zhang, C.; Chen, Y. Deformation control of a symmetric floor heave in deep rock roadway: A case study. *Int. J. Min. Sci. Technol.* **2014**, *6*, 799–804. [CrossRef]
4. Dong, L.; Wang, D.; Sun, X.; Jiang, Y.; Luan, H.; Xu, H.; Li, B.; Cai, F. Large-Deformation Failure Mechanism and Stability Control of a Swelling Soft Rock Roadway in a Sea Area: A Case Study in Eastern China. *Sustainability* **2023**, *15*, 5323. [CrossRef]
5. Zhu, Y.; Tan, Y.; Zhang, S.; Wang, M.; Wang, B. Dynamic Evolution and Quantitative Characterization of Fractures in Coal at the Eastern Edge of Ordos Basin under Axial Loading. *Processes* **2023**, *11*, 1631. [CrossRef]
6. Lv, Y.; Xiao, Q.; Cheng, J. Mechanism and prevention of water-sand inrush in so Mechanism and prevention of water-sand inrush in soft rock with weakly abundant water: A case study in Shanghai miao mining area. *J. China Coal Soc.* **2019**, *44*, 3154–3163.
7. Wang, X.; Wang, X.; Pan, S. Occurrence of analcime in the middle jurassic coal from the Dongsheng coalfield, northeastern Ordos Basin. *China Int. J. Coal Geol.* **2018**, *196*, 126–138. [CrossRef]
8. Srinivasan, C.; Arora, S.; Yaji, R. Use of mining and seismological parameters as premonitors of rock-bursts. *Int. J. Rock Mech. Min. Sci.* **1997**, *34*, 1001–1008. [CrossRef]
9. Torabi, A.; Zarifi, Z. Energy release rate of propagating deformation bands and their hosted cracks. *Int. J. Rock Mech. Min. Sci.* **2014**, *67*, 184–190. [CrossRef]
10. Poulsen, B.; Shen, B.; Williams, D. Strength reduction on saturation of coal and coal measures rocks with implications for coal pillar strength. *Int. J. Rock Mech. Min. Sci.* **2014**, *71*, 41–52. [CrossRef]
11. Petukhov, I.; Linkov, A. The theory of post-failure deformations and the problem of stability in rock mechanics. *Int. J. Rock Mech. Min. Sci. Geomech. Abstr.* **1979**, *16*, 57–76. [CrossRef]
12. Zhou, Y.; Liu, C.; Ma, D.; Zhao, Z. Analysis of strength and acoustic emission characteristics of coal and rock mass in different combinations. *Saf. Coal Min.* **2019**, *50*, 232–236.
13. Chen, G.; Qin, Z.; Zhang, G.; Li, T.; Li, J. Law of energy distribution before failure of a loaded coal-rock combined body. *Rock Soil Mech.* **2020**, *41*, 1–13.
14. Yang, S.; Chen, M.; Jing, H.; Chen, K.; Meng, B. Mechanical properties of rock-coal bi-material samples with different lithologies under uniaxial loading. *Eng. Geol.* **2017**, *217*, 89–101. [CrossRef]
15. Ma, B.; Wang, F.; Liu, H.; Yin, D.; Xia, Z. Mechanical Properties of Rock-Coal-Rock Composites at Different Inclined Coal Seam Thicknesses. *Front. Phys.* **2022**, *9*, 806055. [CrossRef]
16. Song, H.; Zuo, J.; Liu, H.; Zuo, S. The strength characteristics and progressive failure mechanism of soft rock-coal combination samples with consideration given to interface effects. *Int. J. Rock Mech. Min. Sci.* **2021**, *138*, 104593. [CrossRef]
17. Daraei, A.; Sharifi, F.; Qader, D.; Ali, H.; Kolivand, F. Prediction of the static elastic modulus of limestone using downhole seismic test in Asmari formation. *Acta Geoph* **2023**. [CrossRef]
18. Yin, D.; Meng, X. Numerical simulation on uniaxial compression failure of a roof rock-coal-floor rock composite sample with coal persistent joint. *Geotech. Geol. Eng.* **2019**, *37*, 13–23. [CrossRef]
19. Najm, J.; Daraei, A. Forecasting and controlling two main failure mechanisms in the Middle East's longest highway tunnel. *Eng. Fail. Anal.* **2023**, *146*, 107091. [CrossRef]
20. Zuo, J.; Chen, Y.; Cui, F. Investigation on mechanical properties and rock burst tendency of different coal-rock combined bodies. *J. China Univ. Min. Techol.* **2018**, *47*, 81–87.
21. Gong, F.; Ye, H.; Luo, Y. Rate effect on the burst tendency of coal-rock combined body under low loading rate range. *J. China Coal Soc.* **2017**, *42*, 2852–2860.
22. Xie, H. *Introduction to Fractals-Rock Mechanics*; Science Press: Beijing, China, 1996.
23. Chen, G.; Teng, P.; Zhang, G.; Yang, L.; Li, T.; Lv, P. Fractal characteristics and energy transfer mechanism of coal-rock combined body fragments under different loading rates. *J. Chong Qing Univ.* **2022**, *45*, 115–129.
24. Feng, G.; Wen, X.; Guo, J.; Wang, P.; Qian, R.; Yan, Y.; Hao, C. Study on influence of moisture content on coal sample AE properties and fragment distribution characteristics. *J. Cent. South Univ. (Sci. Technol.)* **2022**, *52*, 2910–2918.

25. Li, Y.; Zhang, S.; Wen, Z.; Zhao, R.; Cao, Z.; Lun, Q.; Bai, J. Energy conversion and fragment distribution characteristics of coal sample under uniaxial cyclic loading. *J. China Coal Soc.* **2019**, *44*, 1411–1420.

26. Li, J.; Yan, Z.; Yang, Z.; Fang, W.; Li, T. Evolution and fractal characteristics of uniaxial compression sandstone damage. *Chin. J. Undergr. Space Eng.* **2022**, *18*, 674–682.

27. Zhou, Y.; Yan, Y.; Zhao, K.; Yu, X.; Song, Y.; Wang, J.; Suo, T. Study of the effect of loading modes on the acoustic emission fractal and damage characteristics of cemented paste backfill. *Constr. Build. Mater.* **2021**, *277*, 122311. [CrossRef]

28. Kong, X.; Wang, E.; Hu, S.; Shen, R.; Li, X.; Zhan, T. Fractal characteristics and acoustic emission of coal containing methane in triaxial compression failure. *J. Appl. Geophys.* **2016**, *124*, 139–147. [CrossRef]

29. Fairhurst, C.; Hudson, J. Draft ISRM suggested method for the complete stress-strain curve for intact rock in uniaxial compression. *Int. J. Rock Mech. Min. Sci.* **1999**, *36*, 279–289.

30. Chen, S.; Li, F.; Yin, D.; Zhang, J. Experimental study on deformation failure characteristics of limestone-coal composite with different rock-coal height ratios. *J. Cent. South Univ. (Sci. Techol.)* **2023**, *54*, 2459–2472.

31. Zhou, Z.; Li, X.; Zuo, Y. Fractal characteristics of rock fragmentation at strain rate of 100–102 s^{-1}. *J. Cent. South Univ. (Sci. Techol.)* **2006**, *13*, 290–294. [CrossRef]

32. Rosin, P. The laws governing the fineness of powdered coal. *J. Inst. Fuel* **1933**, *7*, 29–36.

33. Zhao, X.; Xu, S.; Li, Q. Fractal characteristics of fire-damaged ultra high toughness cementitious composite after impact loading. *China Civil Eng. J.* **1933**, *7*, 29–36.

34. Li, C.; Xu, Y.; Zhang, Y.; Li, H. Study on energy evolution and fractal characteristics of cracked coal-rock-like combined body under impact loading. *Chin. J. Rock Mech. Eng.* **2019**, *38*, 2231–2241.

35. Deng, T.; Yang, D.; Hang, W. Influence of loading form on distribution of marble fragments. *J. Tong Ji Univ.* **2007**, *1*, 10–14.

36. Zhu, D.; Jing, H.; Yin, Q.; Han, G. Experimental Study on the Damage of Granite by Acoustic Emission after Cyclic Heating and Cooling with Circulating Water. *Processes* **2018**, *6*, 101. [CrossRef]

37. Yin, J.; Shi, L.; Liu, Z.; Lu, W.; Pan, X.; Zhuang, Z.; Jiao, L.; Kong, B. Study on the Variation Laws and Fractal Characteristics of Acoustic Emission during Coal Spontaneous Combustion. *Processes* **2023**, *11*, 786. [CrossRef]